Deterministic Conductive Filament Formation and Evolution for

Improved Switching Uniformity in Embedded Metal-oxide Based

**Memristor - A Phase Field Study** 

Kena Zhang<sup>1</sup>, P. Ganesh<sup>2</sup>, and Ye Cao<sup>1\*</sup>

<sup>1</sup>Department of Materials Science and Engineering, University of Texas at Arlington, Arlington,

TX, 76019, USA

<sup>2</sup>Center for Nanophase Materials Sciences, Oak Ridge National Laboratory, Oak Ridge, TN

37831, USA

Corresponding author: Ye Cao

\*Email: <u>ye.cao@uta.edu</u>

Phone: +1 8172721858

Address: ELB 332, 501 West First St., Arlington, TX, 76019

#### Abstract

The extreme device-to-device variation of switching performance is one of the major obstacles preventing the applications of metal oxide-based memristors in large-scale memory storage and resistive neural networks. Recent experimental works have reported that embedding metal nano-islands (NIs) in metal oxide can effectively improve the uniformity of the memristors, but the underlying role of the NIs is not fully understood. Here, to address this specific problem, we develop a physical model to understand the origin of the variability and how the embedded NIs can improve the performances and uniformity of memristors. We find that due to dimension confinement effect, embedding metal NIs can modulate the electric field distribution and lead to a more deterministic formation of the conductive filament (CF) from their vicinity, in contrast to random growth of CFs without embedded NIs. This deterministic CF formation, via vacancy nucleation, further reduces the forming, reset, and set voltages, and enhances the uniformity of the operation voltages and current ON/OFF ratios. We further demonstrate that modifying the shapes of the metal NIs can modulate the field strengths/distributions around the NIs, and that choosing NI metal composition and shape that chemically facilitate vacancy formations can further optimize the CF morphology, reduce operation voltages, and improve switching performance. Our work thus provides a fundamental understanding of how embedded metal NIs improve the resistive switching performance in oxide-based memristors and could potentially guide the selection of embedded NIs to realize a more uniform memristor that also operates at higher efficiency than present materials.

Keywords: embedded structure, resistive switching, conductive filament, uniformity, phase-field simulation

## 1. Introduction

Metal oxide based resistive random-access memory (RRAM) exhibits a number of appealing advantages including fast switching speed <sup>1</sup>, low power consumption <sup>2</sup>, good endurance of approximately 10<sup>12</sup> cycles <sup>3</sup>, high scalability <sup>4</sup>, and good compatibility with traditional complementary metal-oxide-semiconductor (CMOS) technology 5, which is considered as one of the most competitive candidates for next generation nonvolatile memory <sup>6</sup>. Especially, the RRAM cell can be integrated into a passive crossbar array to build a resistive neural network and implement neuromorphic computing <sup>7</sup>. A typical RRAM consists of an electrically insulating metal oxide layer, sandwiched by top and bottom electrodes. In general, the fabricated RRAM device is in the insulating state and requires an initial electroforming operation to form oxygen vacancy  $(V_0^-)$  rich conductive filaments (CFs) in the oxide layer. The switching between a high resistance state (HRS) and a low resistance state (LRS) stems from the rupture and reconnection of CFs, which corresponds to the reset and set operations under the applied voltages 8. However, due to the difficulty in fabricating high-quality thin film layer, the synthesized metal oxide devices always suffer from stochasticity in operation voltages, current ON/OFF ratios, and switching speed etc. among different devices, or in the same device among different switching cycles 9, which is one of the critical challenges limiting the widespread application in next generation memory and neuromorphic computing applications. These stochasticity mainly stems from two major reasons: (a) the complex nature of electrode/oxide interface <sup>10</sup>, and (b) the variable chemical properties of the complicated microstructure of metal oxide layer 11. These stochastic properties influence both the electroforming process and the subsequent resistive switching behavior. Extensive experimental studies have been made to understand the stochasticity in RRAMs. For example, Nandi *et al.* <sup>10a</sup> investigated the effect of roughness of electrodes on the electroforming in HfO<sub>2</sub> memristor. They found that the roughness increases the variability of CF position and composition. On the other hand, disorder structures such as grain boundaries, defect clusters show various properties which strongly affect the CF growth during electroforming <sup>11b, 12</sup>. Consequently, the large device-to-device and cycle-to-cycle variations of the RRAMs induced by uncertainty, instability, and non-uniformity of CFs has become the most critical challenge that inhibits the applications of RRAM in large scale memory storage and neuromorphic computing <sup>13</sup>. Therefore, to improve the uniformity and stability of the RRAM devices, effectively controlling the CF formation and rupture is of key importance.

To date, a variety of strategies have been proposed to control the CFs, including the electrode modifications <sup>14</sup> and the switching layer optimizations <sup>14d, e, 15</sup>. It has been reported that fabricating an electrode with pyramid tips rather than a flattened electrode with random roughness could lower the operation voltages and improve the uniformity of RRAM devices <sup>16</sup>. On the other hand, in the switching layer optimization, doping nanoparticles in the metal oxide switching layer have been reported to effectively improve the performance of RRAM devices <sup>15d, e</sup>. Lee *et al.* <sup>17</sup> reported that the current ON/OFF ratio and uniformity were enhanced by dispersing Pt nanoparticles into TiO<sub>2</sub> thin film memristor. Although doping nanoparticles can improve the performance of the RRAM devices to a certain extent, the variable size and random distribution of nanoparticles inside the switching layer inhibit further improvement in the uniformity of RRAM devices. Recently, some researchers have proposed that embedding ordered metal nano-islands (NIs)

within the metal oxide switching layer could be an effective way to overcome the limitation of random nanoparticle doping method. Wang *et al.* <sup>18</sup> employed a template-assisted fabrication approach to embed the ordered metal NIs into the metal oxide thin film, in which the size, interspacing, and thickness of the NIs can be well controlled. The embedded structure can reduce the operation voltages and improve the uniformity of resistance values at HRS and LRS compared to the pristine oxide layer. However, the underlying mechanism of the improvement of the device performance by the embedded structure, and the effects of the composition and geometry of NIs have not been fully understood.

In this study, we develop a comprehensive physical model to study the electroforming and resistive switching behaviors for NIs-embedded HfO<sub>2</sub> based memristor. The current-voltage characteristic, CF morphology, and current ON/OFF ratio of both random and embedded RRAM devices during electroforming and resistive switching processes are systematically explored. Our model clearly reveals that the initial nonuniform  $V_0$  defect distribution is responsible for the stochasticity of CFs formation during the electroforming process, which leads to large variations in operation voltages and current ON/OFF ratios. This nonuniformity can be significantly reduced by the embedded metal NIs due to its confinement effect, i.e., the local field enhancement and promotion of local oxygen vacancy formation. In addition, our model also demonstrates that the height, shape, and composition of metal NIs profoundly influence the resistive switching behavior, implying a materials selection and design strategy of the metal NIs for further improvement of the RRAM uniformity and performance.

# 2. Experimental

## Phase Field Model

In this work, we develop a phase field model to quantitatively describe the electroforming and resistive switching behavior by using  $HfO_{2-x}$  as a prototypical model system. During the electroforming process, the  $V_0^{...}$  are generated and eventually form the CFs that connect the top and bottom electrodes. After electroforming process, the subsequent reset and set processes are controlled by the  $V_0^{...}$  transport in the oxide layer driven by the local electric field and temperature  $^{19}$ . Due to the key role of  $V_0^{...}$  in these processes, we choose oxygen vacancy density  $(N_{V_0^{...}})$  as the order parameter in the phase-field model. The total free energy of the system consists of a electric free energy  $(f_{elec})$  and a chemical energy  $(f_{chem})$ , the latter of which is determined by the thermodynamic equilibrium between oxygen vacancies and oxygen sites by considering the contribution of enthalpy in a dilute solution model  $^{20}$ . Based on this, we describe the transport of  $V_0^{...}$  with a Nernst-Planck equation for charge flux,

$$\frac{\partial N_{V_{\ddot{o}}}}{\partial t} = -\nabla \cdot J_{V_{\ddot{o}}} + G = \nabla \cdot \left( D \nabla N_{V_{\ddot{o}}} + \frac{e_0 D}{k_B T} N_{V_{\ddot{o}}} \nabla \varphi \right) + G \tag{1}$$

where D is the diffusivity of  $V_0^-$  which is described as  $D = D_0 e^{-\frac{E_A}{kT}}$ . Here  $D_0$  is the preexponential factor of diffusivity, and  $E_A$  is the activation energy for  $V_0^-$  migration,  $k_B$  is the Boltzmann constant, T is the temperature,  $e_0$  is the elementary charge,  $\varphi$  is the electrical potential,  $e_0$  and  $e_r$  are the vacuum permittivity and relative permittivity, respectively. G is the generation term during electroforming and set processes. In general, there are two main sources of  $V_0^-$  generation. First, the  $V_0^-$  are likely to be created from the Frenkel pair inside the bulk of the oxide layer when the electrodes are inert metals or compounds, such as TiN and Pt <sup>21</sup>. The formation reaction is expressed in the Kröger-Vink notation as follows,

$$0_0^{\times} \to V_0^{-} + 2e' + \frac{1}{2}O_{2(g)}$$
 (2)

Second, the  $V_0$  can be induced at the active metal/oxide interface by extracting the oxygen atoms from oxide based on the following chemical reaction, which is usually observed in systems using an active metal with high oxygen affinity as the anode electrode, such as Ti, Ta, Hf<sup>22</sup>.

$$M_{\text{active}} + HfO_2 \rightarrow MO_{\delta} + HfO_{2-\delta} + \delta V_{o} + 2\delta e'$$
 (3)

where  $O_0^{\times}$  denotes the lattice oxygen,  $M_{\text{active}}$  stands for the active metal. The bulk generation rate of  $V_0^{\cdot \cdot}$  at the interior of the oxide is determined by  $^{23}$ ,

$$G_{bulk} = G_1 \cdot \left[ \exp\left(\frac{-(E_f - \gamma E)}{k_B T}\right) \right]$$
 (4)

The interface generation rate has a similar form <sup>24</sup>,

$$G_{inter} = G_2 \cdot \left[ \exp\left(\frac{-(E_b - \gamma E)}{k_B T}\right) \right]$$
 (5)

where  $G_1$  and  $G_2$  are the pre-exponential factors for bulk and interface generation rates, respectively,  $\gamma$  is the bond polarization factor, E is the local electrical field. The bulk vacancy formation barrier  $E_f$  represents the capacity of the Frenkel pair generation inside the oxide. The interface vacancy formation barrier  $E_b$  indicates the ability of a metal to extract oxygen atoms from the HfO<sub>2</sub>, which is determined by the properties of metal materials. For simplicity, we ignore the  $V_0$  generation at the electrode/oxide interface

assuming that Pt electrodes are inert. The detailed procedure for the derivation of Eq. (1) from free energy density can be found in Supporting Information Note 1.

The current continuity equation and Fourier heat-flow equation have been solved to determine the local electric potential and temperature,

$$\nabla \cdot \sigma \nabla \varphi = 0 \tag{6}$$

$$-\nabla \cdot k_{th} \nabla T = \sigma |\nabla \varphi|^2 \tag{7}$$

where  $\sigma$  and  $k_{th}$  are the electrical and thermal conductivity. The total current (I) is calculated by a cross-section integral,

$$I = \int \sigma \nabla \varphi \, ds \tag{8}$$

Therefore, we solve three self-consistent partial differential equations (PDEs) including 1) the time-dependent Nernst-Planck equation for  $V_o$  formation and migration, 2) the current continuity equation for electronic conduction, and 3) the Fourier equation for Joule heating using a numerical solver (COMSOL Multiphysics) to calculate the oxygen vacancy density ( $N_{V_o}$ ), electrical potential ( $\varphi$ ), and temperature (T), respectively. Furthermore, with this model we can precisely capture the current-voltage characteristics during the electroforming and resistive switching processing in HfO<sub>2</sub>-based memristors under voltage sweep pulse operation mode. The simulation geometry with radial coordinate r and axial coordinate r, as shown in Figure S1a. The total simulation size is  $60\times60$  nm<sup>2</sup> and the extremely fine physical controlled mesh size is chosen for simulation. The 10-nm-thick HfO<sub>2</sub> film is sandwiched between two 25-nm-thick Pt electrodes. The

external electric voltage ( $V_{\rm app}$ ) is applied to the top electrode, while the bottom electrode is grounded. The temperature at the outmost surfaces of two electrodes is defined with the boundary conditions T=300 K. Zero migration flux  $J_{V_0}$  and generation flux G are assumed at the oxide/electrode interfaces. The detailed equations can be found in Supporting Information Note 1 and the input parameters used in the model are listed in Table S1.

#### 3. Results and discussions

## 3.1 Resistive switching behaviors for random and embedded RRAMs

To understand the influence of metal NIs on the performance of the device, we simulate the electroforming and switching behaviors in HfO<sub>2</sub> memristors with both random structure and embedded structure. We assume that a small number of  $V_0^-$  clusters are randomly dispersed in the HfO<sub>2</sub> layer, which is designated as the initial random structure. The local density of the pre-existing  $V_0^-$  in the defect cluster region is assumed to be  $1.2 \times 10^{27}$  m<sup>-3</sup>, whereas the stoichiometric HfO<sub>2</sub> region has a lower density of  $1.0 \times 10^{15}$  m<sup>-3</sup>. The embedded structure is designated by embedding Pt NIs (d = 6 nm, h = 3 nm) into the HfO<sub>2</sub> thin film with the same initial  $V_0^-$  distribution, as shown in Figure 1b. Then, a negative electric voltage is applied to the top electrode (TE) to perform the electroforming operation and stopped when the current ( $I_{\text{stop}}$ ) reaches 200  $\mu$ A. After that, a triangular voltage sweep with rate dV/dt = 1 V/s is applied to realize the resistive switching process.

Figure 1c shows the calculated current-voltage characteristics of HfO<sub>2</sub> RRAMs based on the phase field model. During the electroforming process, the total currents of both random and embedded structures gradually increase until the applied voltage reaches the forming voltage ( $V_f$ ), followed by a sudden increase of current for more than one order of magnitude, indicating the completion of the electroforming process. After that, the devices are switched from LRS to HRS under the application of a positive bias on TE (the reset process) and switched back to LRS under negative bias (the set process). It is noted that the embedded metal NIs effectively reduces the  $V_f$  from 1.82 V to 1.53 V and  $V_{set}$  from 1.22 V to 0.90 V, and slightly lower the  $V_{reset}$  from 0.81 V to 0.67 V.

The different switching behaviors between the random and embedded structures are likely due to the nature of CF formed during the electroforming process. Therefore, we study the distributions of oxygen vacancy density  $N_{V_0}$ , electrical field E, and temperature T for both random and embedded devices at the forming state (points A and B marked in Figure 1c). When a negative voltage is applied on the random device, the electric field distribution becomes inhomogeneous (snapshot 3 in Figure 1a). It is seen that the electric field above and below the initial oxygen vacancy cluster is enhanced, while the electric field inside the oxygen vacancy clusters is much smaller than that in the vicinity of clusters. This is because the defect cluster has higher electric conductivity than the stoichiometric HfO<sub>2</sub> region. Especially, the electric field is even larger in the local region with closely spaced  $V_0^{..}$  defects. The electric field enhancement further leads to the localized heat generation based on Joule heating (snapshot 4 in Figure 1a). Higher local electric field and temperature promote the  $V_0$  generation rate, resulting in many Frenkel pairs formation here. Thus, while multiple initial  $V_0$  clusters are distributed in the HfO<sub>2</sub> layer, a main CF growth is formed at the position where the initial oxygen vacancies are vertically concentrated (snapshot 2 in Figure 1a). After embedding the Pt NIs with higher electric conductivity  $(1 \times 10^7 \text{ S m}^{-1})$  into the HfO<sub>2</sub> layer with random oxygen vacancies, a higher electrical field concentration at the top and bottom edges of metal NIs is generated (snapshot 3 in Figure 1b). It is interesting to note that CFs form in specific regions pre-determined by the NI position. Additionally, it is also demonstrated that the  $V_o$  density is enhanced almost six orders of magnitude higher than the initial state after the electroforming process. However, in comparison to the embedded device, the oxygen vacancy distribution inside the CF in the random device is inhomogeneous, as shown in Figure S2. The temperature in the

vicinity of the metal NIs is also enhanced (snapshot 4 in Figure 1b). Therefore, the CFs are only formed and aligned in the vicinity of the embedded Pt NIs, due to higher local electric field and temperature than the surrounding area (snapshot 2 in Figure 1b). We further compare the 1D profiles of electrical field and temperature along z direction across the center of NIs and the closely spaced  $V_0$  defects cluster in the embedded device (Line 1,2) in snapshot 3 in Figure 1b). It is seen that the electric field and temperature near the metal NIs are even larger than those around the initial  $V_0$  defect clusters, which favors the  $V_0$ generation in these regions. Eventually, the CFs with uniform morphology preferentially grow along the metal NIs instead of along the initial  $V_0$  clusters. In addition, due to the enhanced electric field by embedding the Pt NIs within the oxide layer, the CF can be formed at a lower voltage, leading to a reduced temperature (~600K) near the CFs in comparison to the random structure (~1200K) (snapshots 4 in Figure 1a and b). Since the high operation voltages and the temperature can cause undesirable crosstalk effects in the memristor crossbar, the reduction in the operation voltages and the temperature with inclusion of NIs benefits the application of memristor based electronic devices <sup>25</sup>.

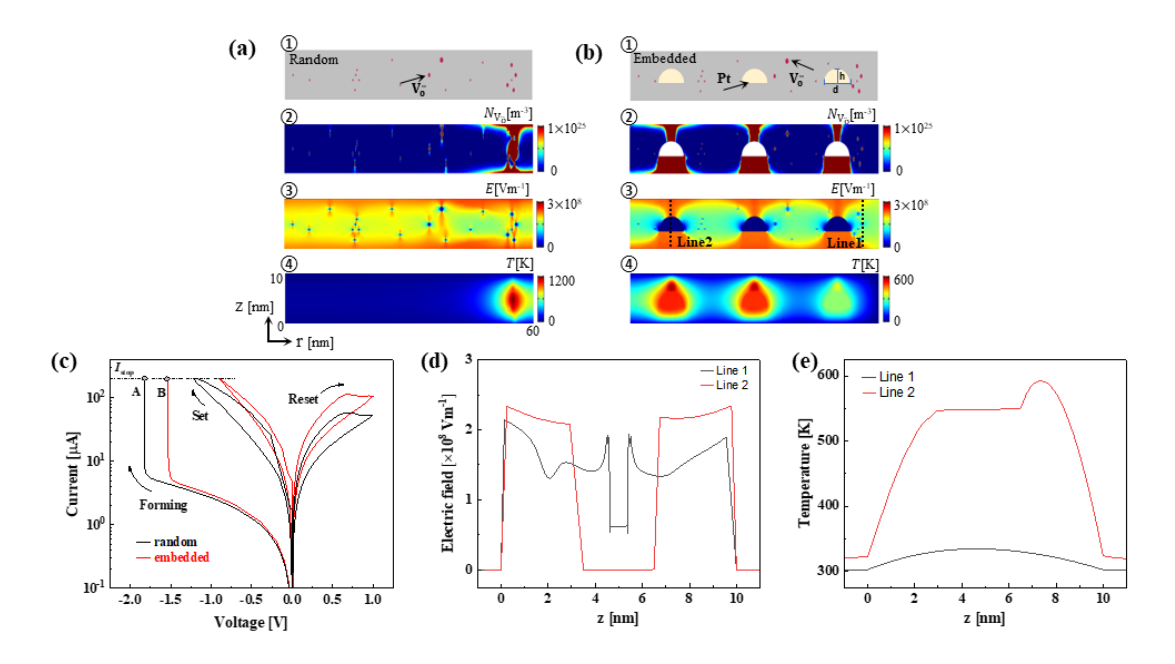


Figure 1 (a, b) The initial structure, 2D maps of oxygen vacancy density  $(N_{V_0})$ , electric field (E), and temperature (T) at forming state for the HfO<sub>2</sub> thin film memristors with (a) random structure and (b) embedded structure. (c) Current-voltage curves. (d, e) 1D profiles of (d) E and (e) T across the center of defect cluster (Line 1) and embedded NI (Line 2) marked as the dot lines in snapshot 3 in (b) at the forming state for the embedded structure.

After the electroforming process, a positive triangle voltage is applied on the TE to perform the reset process. Under the applied voltage, the  $V_0^{-}$  in the CF migrate from the TE to BE and the CF ruptures near TE for both random and embedded structures, as shown in Figure 2a and b. The 1D electric field and local temperature distributions along the center of the CFs at the final reset states ( $V_{app} = 1 \text{ V}$ ) in both random structure (Line 1 in Figure 2a) and embedded structure (Line 2 in Figure 2b) are shown in Figure 2c and d. Compared with the random case, we observe a local electric field enhancement in the embedded device, which thereby increases the driving force for  $V_0^{-}$  migration towards BE, lowering the reset voltage and increasing the current ON/OFF ratio. Details can be found in Table S2. After reset switching, the CF is broken above the NIs, while some residual oxygen-rich regions remain. Therefore, the subsequent set process requires a lower voltage than the

initial electroforming process (Figure 1c). Also, the embedded NI serves as an electric concentrator and facilitates the  $V_0$  generation similar to the electroforming process, in which the  $V_{\text{set}}$  for embedded structure is smaller than that for random structure (Figure 1c).

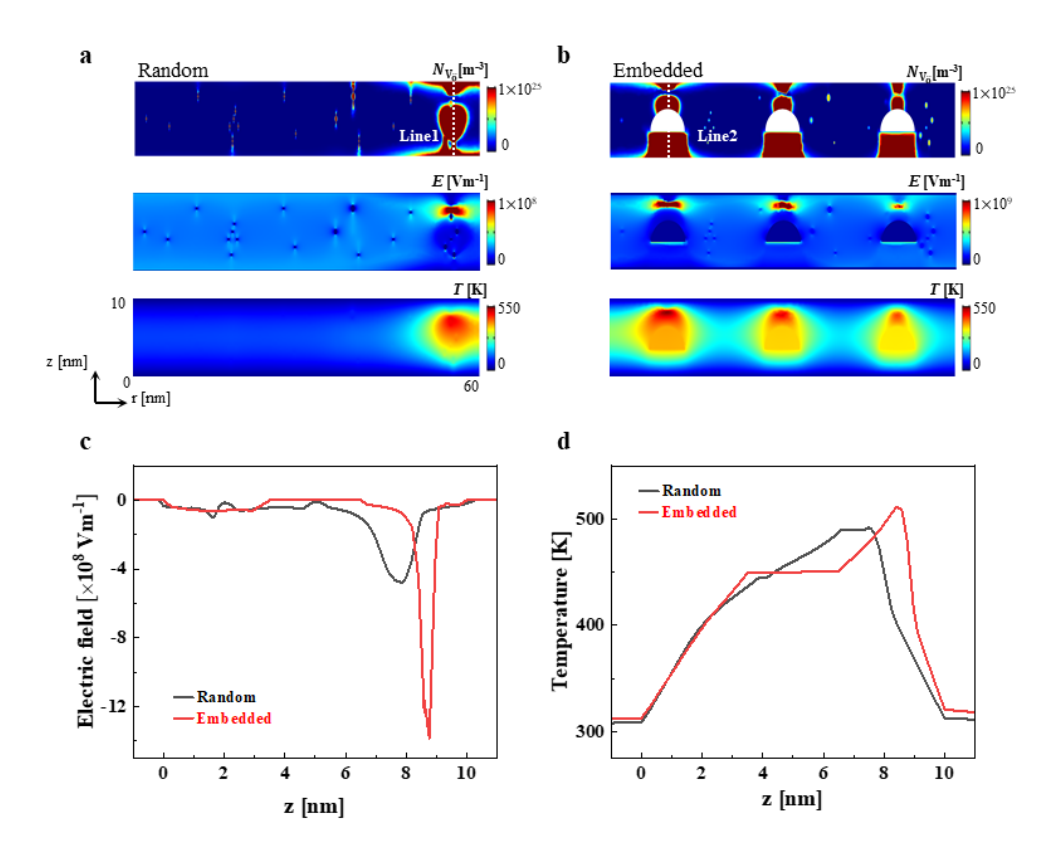


Figure 2 (a, b) 2D maps of oxygen vacancy density  $N_{V_0^*}$ , electric field (E) and temperature (T) at reset state ( $V_{\rm app} = 1 \text{ V}$ ) in the (a) random structure and (b) embedded structure. (c, d) 1D profiles of (c) E and (d) T at reset state across the center of CF in the random structure and embedded structure marked as the dot lines in (a) and (b).

# 3.2 The improvement of the uniformity of embedded RRAMs

Our simulation results indicate that the initial oxygen vacancy density and distribution strongly affect the CF growth, however, the initial defect within the deposited HfO<sub>2</sub> thin film is unpredictable and uncontrollable due to the limitations of the synthesis process. To understand the effects of the embedded NIs on confining the CF formation, we

simulate the forming and switching behavior of both random and embedded devices. For simplicity, we only simulate three different random devices which contain different initial distributions of the  $V_o$  clusters while keeping the total number of  $V_o$  constant in the HfO<sub>2</sub> film (snapshots Init rm 1-3 in Figure 3a-c). The corresponding embedded devices are obtained by embedding Pt NIs into each random device (snapshots Init emb 1-3 in Figure 3a-c). After the electroforming process, we find that the CFs are formed in different morphologies and at various positions. In some cases, a secondary sub-filament connected to TE and BE electrodes is formed within the HfO<sub>2</sub> layer (snapshot rm2 in Figure 3b). The complexity of the morphologies and locations of the CFs due to the initial random microstructure could well explain the instability and variability in RRAMs for both forming, reset, and set processes. In contrast to the stochastic formation of CFs in random devices, the CFs generated in the embedded devices show much better uniformity. As snapshot emb1-3 shown in Figure 3a-c, three separately ordered CFs with uniform morphology and specific locations are formed in the vicinity of metal NIs, regardless of the initial random structure of  $V_0$  clusters. In addition, embedding NIs also significantly reduces the device-to-device variability. As shown in Figure 3d, various operation voltages are found in different random HfO<sub>2</sub> devices. Especially, the forming/set voltages often experience higher variability than the reset voltages, which are usually observed in many experimental works <sup>9a, 15c</sup>. In contrast, for the three embedded devices, the I-V curves and the operation voltages are almost identical (Figure 3e). Figure 3f compares the variations of operation voltages and the corresponding current ON/OFF ratios for both random and embedded devices. From Figure 3f and Table S2, two distinct trends are observed. First, the embedded metal NIs can reduce the  $V_{\rm f}$ ,  $V_{\rm reset}$ ,  $V_{\rm set}$  by 16%, 17%, and 28% on average,

and enhance the  $I_{\rm on}/I_{\rm off}$  by an average of 30.8%, compared to the random structure. Second, the introduction of NIs effectively reduces the variations in operation voltages and  $I_{\rm on}/I_{\rm off}$ , as the red dots shown in Figure 3f. To quantify these changes, we introduce a coefficient of variation (CV, defined as the ratio of the standard deviation ( $\delta$ ) to the mean value ( $\mu$ )), and the detailed statistical data is shown in Table S2 in the SI. The embedded devices show a significant uniformity in comparison with random structures, in which the CV of  $V_f$ ,  $V_{reset}$ , and  $V_{\text{set}}$  are reduced by 97%, 63%, and 80%, respectively. Moreover, the embedded NIs significantly reduce the CV of  $I_{\rm on}/I_{\rm off}$  from 17.8% for random devices to 3.8%. The large device-to-device variation in device characteristics can significantly impact the accuracy and efficiency of machine learning applications by using a resistive switching based neural network<sup>26</sup>. In particular, voltage variation in resistive switching devices is fatal to programming accuracy, and it should be well controlled <sup>4</sup>. Our findings highlight that embedding metal NIs inside the stochastic HfO<sub>2</sub> thin film can achieve highly controllable CF formation, and especially enhance the uniformity of both operation voltages and current ON/Off ratio in metal oxide-based RRAMs. These embedded devices with high uniformity show great potential in the application of artificial neural networks <sup>13b, 25</sup>.

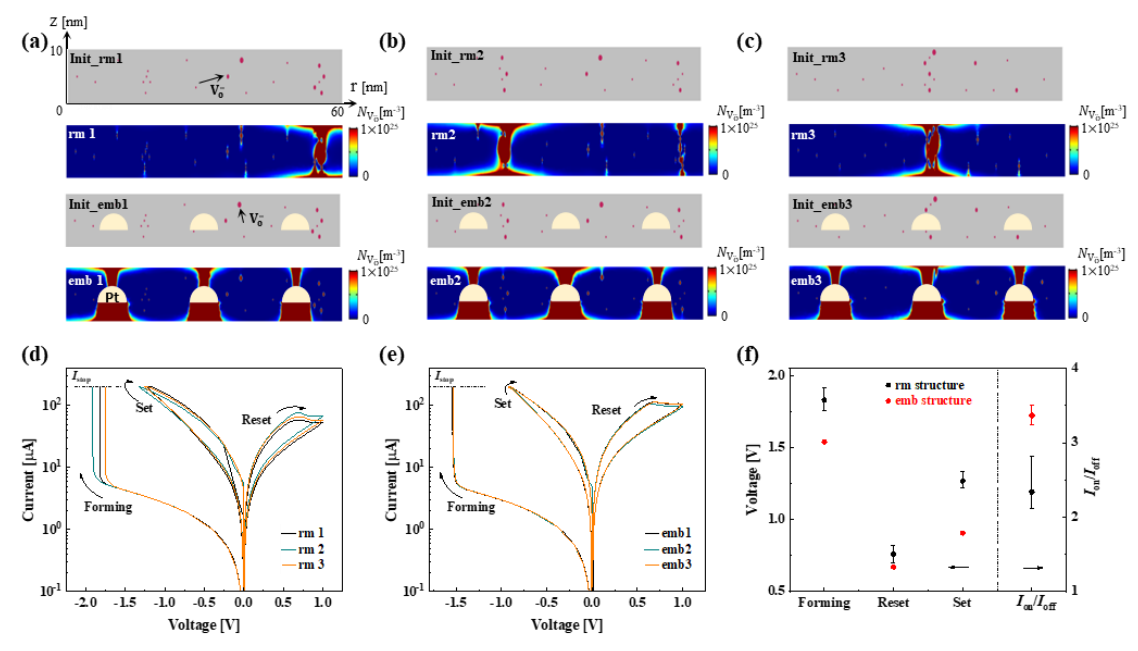


Figure 3 (a-c) Three different initial random structure (Init\_rm 1-3) and the embedded structure (Init\_emb 1-3) and the corresponding 2D maps of  $N_{V_0^{"}}$  at forming state. (d, e) Current-voltage curves for (d) the random structures (rm 1-3) and (e) embedded structures (emb 1-3). (f) The variations of the voltage and current ON/OFF ratio ( $I_{on}/I_{off}$ ) for the random and embedded structures.

# 3.3 Effect of the height, geometry, and materials properties of the metal NIs

According to the previous results, the NIs act as the electric field concentrator and play an important role in the formation and rupture of CFs. Here, we further investigate the effect of the height, geometry, and material properties of the metal NIs on the CF growth and the switching behaviors. For simplicity, we ignore the initial pre-existing  $V_0$  defects within the HfO<sub>2</sub> layer and introduce only one embedded NI. Figure 4a and b illustrate the effect of NI's height on the CF morphology and I-V characteristics. It is found that  $V_f$ ,  $V_{reset}$ , and  $V_{set}$  all decrease when h increases. That is because the effective thickness of HfO<sub>2</sub> along the vertical region of the NI decreases accordingly as h increases. Therefore, the local electric field above and below the NI is further enhanced. As shown in Figure 4c, the maximum electric field has doubled when h increases from 1 nm to 5 nm under the same applied voltage ( $V_{app} = -1$  V) during the electroforming process (point A in Figure 4b). The

enhancement of local electric field promotes the  $V_0$  generation in the vicinity of NI which eventually decreases the forming and set voltages. During the reset process, the maximum local electric field and temperature near TE gradually increase when the height of NI increases, which promotes the  $V_0$  migration from TE to BE (see Figure S3b and c in SI). Therefore, embedding NI with increasing height in the HfO<sub>2</sub> switching layer leads to an effective reduction in reset voltages and a significant increase in the  $I_{on}/I_{off}$  ratio, as shown in Figure 4a and Table S3.

We also investigate the effect of the NI's geometry on the switching performance by changing the shapes of NIs (rectangle, semicircle, and triangle, Figure 4d), while keeping both the area size and height of NIs to be constant. As shown in Figure 4e and Table S3, different geometry of NIs has almost no effect on the forming and set voltages, although the triangle NIs can reduce the reset voltage and enhance the  $I_{on}/I_{off}$  ratio compared to others, due to its sharp corners that naturally host higher electric fields. Fig. 4f compares the electric field distributions along the center of CF for different geometry of NIs during electroforming ( $V_{\rm app} = -0.5 \,\rm V$ ). It is found that the electric field enhancement above and below the NI are symmetric for rectangle NI, while it is highly asymmetric for triangle NIs with a local field concentration on top of the triangle tip. This locally enhanced field accelerates the  $V_0$  generation and causes a local  $V_0$  enhancement at the tip of the triangle NI compared with semicircle and rectangle NIs (Figure 4g). The formed CF with higher  $V_0$  density at the tip of the triangle NI exhibits a higher electric conductivity. Thus, the locally enhanced electric field and temperature above the triangle NI tip are higher than those in other NI geometries during the reset operation (Figure S4b and c), which promotes the  $V_0$  migration from TE to BE. Therefore, the corresponding  $V_{\text{reset}}$  is decreased and the  $I_{\text{on}}/I_{\text{off}}$  ratio is enhanced by embedding triangle NI (Figure 4e and Table S3).

Finally, we investigate the effect of material types of embedded metallic NIs on the resistive switching behavior. In the previous simulation, we ignored the  $V_0$  exchange at the electrode/oxide and oxide/NI interfaces (i.e., Pt/HfO<sub>2</sub> interfaces) due to the low oxygen affinity of the inert Pt, and we assume that the  $V_0$  are generated only from the Frenkel pairs inside the bulk of HfO<sub>2</sub> oxide (Eq. (2)). However, many recent works demonstrate that some active metals can also extract the oxygen atom from the oxide switching layer <sup>18, 22c</sup>, which provides an additional  $V_0$  generation source (Eq. (3)). The  $V_0$  generation rate at the interface of metal/oxide is strongly dependent on the metal properties, i.e., the ability to extract oxygen atoms from  $HfO_2$  indicated by the interface vacancy formation energy  $E_b$ . To fully understand the role of different metal NIs in the electroforming and switching processes, we select the metal Ti, Ta, and Pt as candidates of the embedded metal NIs with increasing  $E_b$  of 0.6, 2.5, and 8.5 eV, respectively  $^{22c}$ , and incorporate the  $V_o$  generation from both bulk Frenkel pair and replacement reaction at the metal oxide/NI interface, with corresponding generation rates determined by Eq. (4) and Eq. (5). Figures 4h and S5 demonstrate the 2D map and the 1D profile of V<sub>o</sub> density distribution across the center of CF at the forming state for different oxide NIs devices. The I-V curves are shown in Figure 4i. Figure 4j compares the  $V_o$  generation rates at different HfO<sub>2</sub>/NIs interfaces during the electroforming process. As the active  $Ti_NI$  exhibits a very large interface  $V_o$  generation rate, a significant number of  $V_o$  can be generated at the Ti/HfO<sub>2</sub> interface. Consequently, the CF with higher  $V_o$  concentration and wider width is formed at a small voltage for the HfO<sub>2</sub>\_Ti device (Figure S5 and 4i). Furthermore, the interface  $V_o$  generation rate is

suppressed as  $E_b$  increases (Figure 4j). Especially for inert embedding Pt\_NIs with a large vacancy formation barrier ( $E_b = 8.5 \text{ eV}$ ), almost no  $V_0$  are generated near the oxide/Pt\_NI interface, and the embedded Pt\_NI only displays the electric field concentration effect. Figure 4k shows the average  $V_0$  density along the center of the CF (r = 10,  $z = 0 \sim 10$  nm) at the forming state. It is also found that the average  $V_0$  density along the center of CF of Ti\_NI embedded device reaches  $2.32 \times 10^{26} \text{ m}^{-3}$ , which is almost ten times of that in Pt\_NI embedded device (Figure 4k). Due to the high density of  $V_0$  in the Ti\_NI embedded devices, the formed CF exhibits a higher electric conductivity. Therefore, for the subsequent reset process, the maximum local electric field and temperature for Ti\_NI embedded device are larger than the others (Figure S6b and c), which further promotes the  $V_0$  drift to BE to form a wider  $V_0$  depletion gap near TE, and lowering the reset voltages and enhancing the  $I_{on}/I_{off}$  ratio (Table S3). Therefore, selecting metallic NIs of lower  $V_0$  formation barrier within the host oxide is ideal to realize controllable CF growth at a much smaller operation voltage.

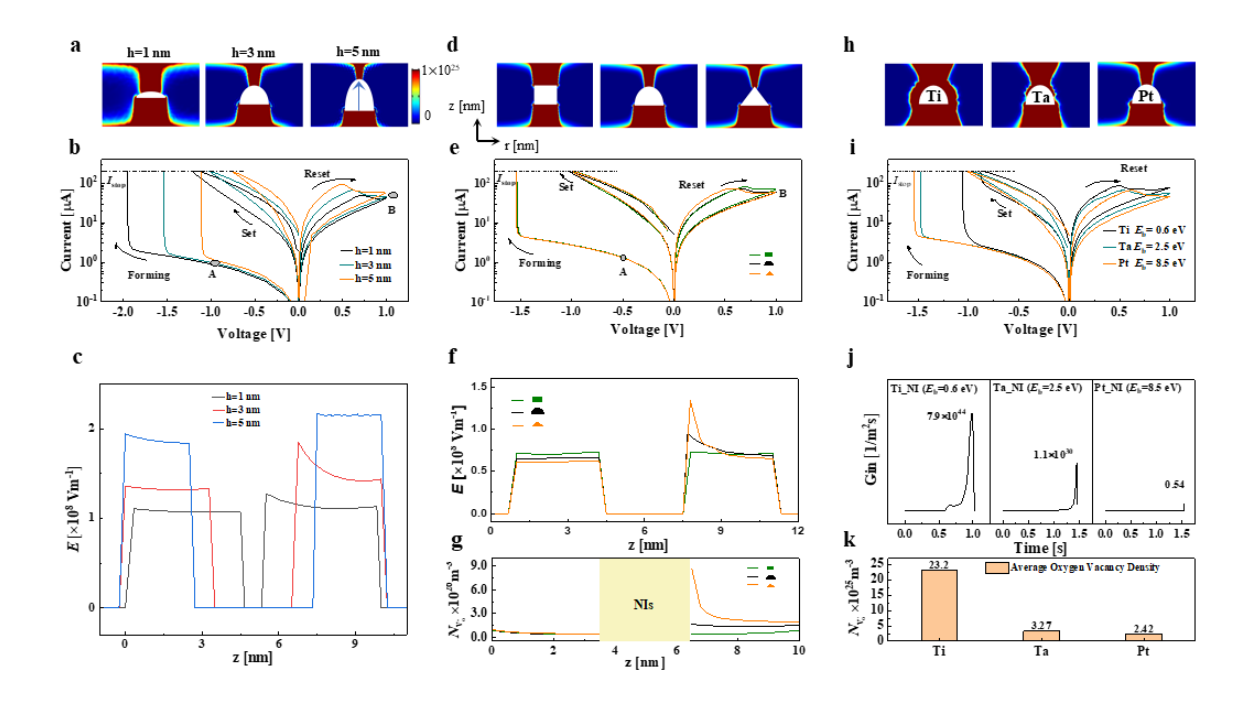


Figure 4 The effect of the height, geometry, and materials properties of the embedded metal NIs on switching performance. (a) 2D maps of  $N_{V_0^{"}}$  at forming state and (b) Current-voltage curves for devices embedding metal NIs with different height. (c) The electric field along the center of CF (r=10 nm,  $z=0\sim10$  nm) at  $V_{\rm app}=-1.0$  V during the forming process, corresponding to the state A in (b); (d) 2D maps of  $N_{V_0^{"}}$  at forming state and (e) Current-voltage curves for devices embedding metal NIs with different geometry. (f) The electric field and along the center of CF at  $V_{\rm app}=-0.5$  V during the forming process, corresponding to the state A in (e). (g) 1D profiles of  $N_{V_0^{"}}$  along the center of CF at forming state; (h) 2D maps of  $N_{V_0^{"}}$  at forming state and (i) Current-voltage curves for devices embedding metal NIs with different materials. (j) The interface generation rate at different metal NIs/oxide interfaces during electroforming process. (k) The average  $N_{V_0^{"}}$  along the center of CF at the forming state.

#### 4. Conclusions

In this study, a physical model is developed to understand the dynamic switching process including electroforming, reset, and set cycle in RRAM devices. It is found that the stochasticity in the CF growth during the electroforming process arises from the unpredictable and uncontrollable initial  $V_0$  defect clusters, which act as the CF formation seeds. Embedding NIs could enhance the electrical field above and below the NIs, which promotes the  $V_0$  generation and accumulation in the vicinity of NIs rather than surrounding the initial defect clusters, and realizes the controllable CF growth. This effect can be sufficiently enhanced by embedding triangular NIs that have a higher field at its corners. This results in the embedded metal NIs reducing the operation voltages and enhancing the device-to-device uniformity in terms of operation voltages and  $I_{\rm on}/I_{\rm off}$  ratio. In addition to enhancing the fields by altering the shape, increasing the height of NIs, or using active metal NIs with smaller  $E_b$  could also further reduce the operation voltages and enhance the  $I_{\rm on}/I_{\rm off}$  ratio. Our work provides a comprehensive understanding of the effect of embedding NIs on the CF formation and rupture during switching, and how it can be utilized to optimize the RRAM device variability, which can be employed to guide the experimental design of future memristors with high uniformity.

ASSOCIATED CONTENT

**Supporting Information** 

Detailed description of phase field simulation model (geometry, equations, and parameters),

Statistic performance data of random and embedded RRAM devices including the

operation voltages and current ON/OFF ratio. Simulation results of HfO<sub>2</sub> films embedding

Pt NI with different height, geometry, and materials during reset process.

AUTHOR INFORMATION

Corresponding author

Ye Cao -- Department of Materials Science and Engineering, University of Texas at

Arlington, Arlington, TX, 76019, USA

Email: ye.cao@uta.edu

**Authors** 

Kena Zhang -- Department of Materials Science and Engineering, University of Texas at

Arlington, Arlington, TX, 76019, USA

P. Ganesh -- Center for Nanophase Materials Sciences, Oak Ridge National Laboratory,

Oak Ridge, TN 37831, USA

**Author Contributions** 

Y. C. conceived the idea and constructed the research framework. K. Z. performed the

simulations and wrote the manuscript. All authors discussed the results and commented on

the manuscript.

**Competing Financial Interest** 

The authors declare no competing financial interest.

23

# **Declaration of Competing Interest**

The authors declare that they have no known competing financial interests or personal relationships that could have appeared to influence the work reported in this paper.

# Acknowledgements

K.Z. and Y.C. and acknowledges the support from the National Science Foundation (NSF) under the award number NSF 2132105. P.G. (physical model, analysis and interpretation) was supported by the Center for Nanophase Materials Sciences, which is a DOE Office of Science User Facility.

## Reference

- 1. Zhang, C.; Liu, G.; Geng, X.; Wu, K.; Debliquy, M., Metal oxide semiconductors with highly concentrated oxygen vacancies for gas sensing materials: A review. *Sens. Actuator A Phys.* **2020**, *309*, 112026.
- 2. Yang, J. J.; Strukov, D. B.; Stewart, D. R., Memristive devices for computing. *Nat. Nanotechnol.* **2013**, *8* (1), 13-24.
- 3. Carlos, E.; Branquinho, R.; Martins, R.; Kiazadeh, A.; Fortunato, E., Recent progress in solution-based metal oxide resistive switching devices. *Adv. Mater.* **2021**, *33* (7), 2004328.
- 4. Xia, Q.; Yang, J. J., Memristive crossbar arrays for brain-inspired computing. *Nat. Mater.* **2019**, *18* (4), 309-323.
- 5. (a) Pi, S.; Li, C.; Jiang, H.; Xia, W.; Xin, H.; Yang, J. J.; Xia, Q., Memristor crossbar arrays with 6-nm half-pitch and 2-nm critical dimension. *Nat. Nanotechnol.* **2019**, *14* (1), 35-39; (b) lelmini, D., Resistive switching memories based on metal oxides: mechanisms, reliability and scaling. *Semicond. Sci. Technol.* **2016**, *31* (6), 063002.
- 6. (a) Celano, U.; Goux, L.; Degraeve, R.; Fantini, A.; Richard, O.; Bender, H.; Jurczak, M.; Vandervorst, W., Imaging the three-dimensional conductive channel in filamentary-based oxide resistive switching memory. *Nano Lett* **2015**, *15* (12), 7970-7975; (b) Yang, Y. C.; Gao, P.; Gaba, S.; Chang, T.; Pan, X. Q.; Lu, W., Observation of conducting filament growth in nanoscale resistive memories. *Nat Commun* **2012**, *3*, 732.
- (a) Ielmini, D., Brain-inspired computing with resistive switching memory (RRAM): Devices, 7. synapses and neural networks. Microelectron. Eng. 2018, 190, 44-53; (b) Wang, Z.; Wu, H.; Burr, G. W.; Hwang, C. S.; Wang, K. L.; Xia, Q.; Yang, J. J., Resistive switching materials for information processing. Nat. Rev. Mater. 2020, 5 (3), 173-195; (c) Ielmini, D.; Wong, H. S. P., In-memory computing with resistive switching devices. Nat. Electron. 2018, 1 (6), 333-343; (d) Ismail, M.; Abbas, H.; Choi, C.; Kim, S., Controllable analog resistive switching and synaptic characteristics in ZrO₂/ZTO bilayer memristive device for neuromorphic systems. Appl. Surf. Sci. 2020, 529, 147107; (e) Yao, P.; Wu, H.; Gao, B.; Eryilmaz, S. B.; Huang, X.; Zhang, W.; Zhang, Q.; Deng, N.; Shi, L.; Wong, H. P.; Qian, H., Face classification using electronic synapses. Nat Commun 2017, 8, 15199; (f) Prezioso, M.; Merrikh-Bayat, F.; Hoskins, B. D.; Adam, G. C.; Likharev, K. K.; Strukov, D. B., Training and operation of an integrated neuromorphic network based on metal-oxide memristors. Nature **2015,** 521 (7550), 61-64; (g) Oh, J.; Yoon, S. M., Resistive Memory Devices Based on Reticular Materials for Electrical Information Storage. ACS Appl Mater Interfaces 2021, 13 (48), 56777-56792; (h) Ge, R.; Wu, X.; Liang, L.; Hus, S. M.; Gu, Y.; Okogbue, E.; Chou, H.; Shi, J.; Zhang, Y.; Banerjee, S. K.; Jung, Y.; Lee, J. C.; Akinwande, D., A Library of Atomically Thin 2D Materials Featuring the Conductive-Point Resistive Switching Phenomenon. Adv Mater 2021, 33 (7), e2007792.
- 8. Jeong, D. S.; Thomas, R.; Katiyar, R. S.; Scott, J. F.; Kohlstedt, H.; Petraru, A.; Hwang, C. S., Emerging memories: resistive switching mechanisms and current status. *Rep. Prog. Phys.* **2012**, *75* (7), 076502.
- 9. (a) You, B. K.; Park, W. I.; Kim, J. M.; Park, K.-I.; Seo, H. K.; Lee, J. Y.; Jung, Y. S.; Lee, K. J., Reliable Control of Filament Formation in Resistive Memories by Self-Assembled Nanoinsulators Derived from a Block Copolymer. *ACS Nano* **2014**, *8* (9), 9492-9502; (b) Ambrogio, S.; Balatti, S.; Cubeta, A.; Calderoni, A.; Ramaswamy, N.; Ielmini, D., Statistical Fluctuations in HfOx Resistive-Switching Memory: Part I Set/Reset Variability. *IEEE Trans, Electron Devices* **2014**, *61* (8), 2912-2919.
- 10. (a) Nandi, S. K.; Liu, X.; Venkatachalam, D. K.; Elliman, R. G., Effect of electrode roughness on electroforming in HfO<sub>2</sub> and defect-induced moderation of electric-field enhancement. *Phys.*

- Rev. Appl. 2015, 4 (6), 064010; (b) Yong, Z.; Persson, K.-M.; Saketh Ram, M.; D'Acunto, G.; Liu, Y.; Benter, S.; Pan, J.; Li, Z.; Borg, M.; Mikkelsen, A.; Wernersson, L.-E.; Timm, R., Tuning oxygen vacancies and resistive switching properties in ultra-thin HfO<sub>2</sub> RRAM via TiN bottom electrode and interface engineering. Appl. Surf. Sci. 2021, 551; (c) Koroleva, A. A.; Chernikova, A. G.; Chouprik, A. A.; Gornev, E. S.; Slavich, A. S.; Khakimov, R. R.; Korostylev, E. V.; Hwang, C. S.; Markeev, A. M., Impact of the atomic layer-deposited Ru electrode surface morphology on resistive switching properties of TaO<sub>x</sub>-based memory structures. ACS Appl. Mater. Interfaces 2020, 12 (49), 55331-55341; (d) Mao, H.; Zhou, Z.; Wang, X.; Ban, C.; Ding, Y.; Sun, T.; Yin, Y.; Liu, Z.; Liu, J.; Huang, W., Control of resistive switching voltage by nanoparticle-decorated wrinkle interface. Adv. Electron. Mater. 2018, 5 (5), 1800503.
- 11. (a) Zhang, F.; Li, X.; Gao, X.; Wu, L.; Zhuge, F.; Wang, Q.; Liu, X.; Yang, R.; He, Y., Effect of defect content on the unipolar resistive switching characteristics of ZnO thin film memory devices. *Solid State Commun.* **2012**, *152* (17), 1630-1634; (b) Lanza, M.; Zhang, K.; Porti, M.; Nafría, M.; Shen, Z. Y.; Liu, L. F.; Kang, J. F.; Gilmer, D.; Bersuker, G., Grain boundaries as preferential sites for resistive switching in the HfO2 resistive random access memory structures. *Appl. Phys. Lett.* **2012**, *100* (12).
- 12. Bersuker, G.; Yum, J.; Vandelli, L.; Padovani, A.; Larcher, L.; Iglesias, V.; Porti, M.; Nafría, M.; McKenna, K.; Shluger, A.; Kirsch, P.; Jammy, R., Grain boundary-driven leakage path formation in HfO<sub>2</sub> dielectrics. *Solid-State Electron.* **2011**, *65-66*, 146-150.
- 13. (a) Yu, S.; Gao, B.; Fang, Z.; Yu, H.; Kang, J.; Wong, H. S., A low energy oxide-based electronic synaptic device for neuromorphic visual systems with tolerance to device variation. *Adv. Mater.* **2013**, *25* (12), 1774-1779; (b) Kim, G. S.; Song, H.; Lee, Y. K.; Kim, J. H.; Kim, W.; Park, T. H.; Kim, H. J.; Min Kim, K.; Hwang, C. S., Defect-Engineered Electroforming-Free Analog HfOx Memristor and Its Application to the Neural Network. *ACS Appl. Mater. Interfaces* **2019**, *11* (50), 47063-47072.
- 14. (a) Jesse, S.; Lee, H. N.; Kalinin, S. V., Quantitative mapping of switching behavior in piezoresponse force microscopy. *Review of Scientific Instruments* **2006**, *77* (7), 073702; (b) Kondo, T.; Lee, S. M.; Malicki, M.; Domercq, B.; Marder, S. R.; Kippelen, B., A Nonvolatile Organic Memory Device Using ITO Surfaces Modified by Ag-Nanodots. *Adv. Funct. Mater.* **2008**, *18* (7), 1112-1118; (c) Shin, M.; Lee, H. S.; Sim, Y. C.; Cho, Y. H.; Cheol Choi, K.; Shin, B., Modulation of Growth Kinetics of Vacuum-Deposited CsPbBr3 Films for Efficient Light-Emitting Diodes. *ACS Appl. Mater. Interfaces* **2020**, *12* (1), 1944-1952; (d) Kim, H. J.; Park, T. H.; Yoon, K. J.; Seong, W. M.; Jeon, J. W.; Kwon, Y. J.; Kim, Y.; Kwon, D. E.; Kim, G. S.; Ha, T. J.; Kim, S. G.; Yoon, J. H.; Hwang, C. S., Fabrication of a Cu-Cone-Shaped Cation Source Inserted Conductive Bridge Random Access Memory and Its Improved Switching Reliability. *Adv. Funct. Mater.* **2019**, *29* (8), 1806278; (e) Chen, Q.; Liu, G.; Xue, W.; Shang, J.; Gao, S.; Yi, X.; Lu, Y.; Chen, X.; Tang, M.; Zheng, X.; Li, R.-W., Controlled Construction of Atomic Point Contact with 16 Quantized Conductance States in Oxide Resistive Switching Memory. *Appl. Electron. Mater.* **2019**, *1* (5), 789-798.
- 15. (a) Yoon, J. H.; Zhang, J.; Ren, X.; Wang, Z.; Wu, H.; Li, Z.; Barnell, M.; Wu, Q.; Lauhon, L. J.; Xia, Q.; Yang, J. J., Truly Electroforming-Free and Low-Energy Memristors with Preconditioned Conductive Tunneling Paths. *Adv. Funct. Mater.* **2017**, *27* (35), 1702010; (b) Liu, Q.; Guan, W.; Long, S.; Jia, R.; Liu, M.; Chen, J., Resistive switching memory effect of ZrO[sub 2] films with Zr[sup +] implanted. *Appl. Phys. Lett.* **2008**, *92* (1), 012117; (c) Yoon, J. H.; Han, J. H.; Jung, J. S.; Jeon, W.; Kim, G. H.; Song, S. J.; Seok, J. Y.; Yoon, K. J.; Lee, M. H.; Hwang, C. S., Highly improved uniformity in the resistive switching parameters of TiO2 thin films by inserting Ru nanodots. *Adv. Mater.* **2013**, *25* (14), 1987-1992; (d) Xu, Z.; Gao, M.; Yu, L.; Lu, L.; Xu, X.; Jiang, Y., Co nanoparticles induced resistive switching and magnetism for the electrochemically deposited polypyrrole composite films. *ACS Appl. Mater. Interfaces* **2014**, *6* (20), 17823-17830; (e) Yoon, J. H.; Kim, K. M.; Lee, M.

- H.; Kim, S. K.; Kim, G. H.; Song, S. J.; Seok, J. Y.; Hwang, C. S., Role of Ru nano-dots embedded in TiO2 thin films for improving the resistive switching behavior. *Appl. Phys. Lett.* **2010**, *97* (23), 232904.
- 16. (a) Shin, K.-Y.; Kim, Y.; Antolinez, F. V.; Ha, J. S.; Lee, S.-S.; Park, J. H., Controllable Formation of Nanofilaments in Resistive Memories via Tip-Enhanced Electric Fields. *Adv. Electron. Mater.* **2016**, *2* (10), 1600233; (b) Kim, Y.; Choi, H.; Park, H. S.; Kang, M. S.; Shin, K. Y.; Lee, S. S.; Park, J. H., Reliable Multistate Data Storage with Low Power Consumption by Selective Oxidation of Pyramid-Structured Resistive Memory. *ACS Appl. Mater. Interfaces* **2017**, *9* (44), 38643-38650; (c) Kim, H. D.; Yun, M. J.; Hong, S. M.; Kim, T. G., Effect of nanopyramid bottom electrodes on bipolar resistive switching phenomena in nickel nitride films-based crossbar arrays. *Nanotechnology* **2014**, *25* (12), 125201.
- 17. Lee, C.; Kim, I.; Shin, H.; Kim, S.; Cho, J., Nonvolatile memory properties of Pt nanoparticle-embedded TiO(2) nanocomposite multilayers via electrostatic layer-by-layer assembly. *Nanotechnology* **2010**, *21* (18), 185704.
- 18. Wang, J.; Li, L.; Huyan, H.; Pan, X.; Nonnenmann, S. S., Highly Uniform Resistive Switching in HfO<sub>2</sub> Films Embedded with Ordered Metal Nanoisland Arrays. *Adv. Funct. Mater.* **2019**, *29* (25), 1808430.
- 19. Kim, S.; Kim, S. J.; Kim, K. M.; Lee, S. R.; Chang, M.; Cho, E.; Kim, Y. B.; Kim, C. J.; Chung, U. I.; Yoo, I. K., Physical electro-thermal model of resistive switching in bi-layered resistance-change memory. *Sci Rep-Uk* **2013**, *3*, 1680.
- 20. Zhang, K.; Wang, J.; Huang, Y.; Chen, L.; Ganesh, P.; Cao, Y., High-throughput phase-field simulations and machine learning of resistive switching in resistive random-access memory. *npj Computational Materials* **2020**, *6* (1), 198.
- 21. (a) Yang, J. J.; Miao, F.; Pickett, M. D.; Ohlberg, D. A.; Stewart, D. R.; Lau, C. N.; Williams, R. S., The mechanism of electroforming of metal oxide memristive switches. *Nanotechnology* **2009**, *20* (21), 215201; (b) Jeong, D. S.; Schroeder, H.; Breuer, U.; Waser, R., Characteristic electroforming behavior in Pt/TiO<sub>2</sub>/Pt resistive switching cells depending on atmosphere. *Journal of Applied Physics* **2008**, *104* (12), 123716; (c) Sharath, S. U.; Joseph, M. J.; Vogel, S.; Hildebrandt, E.; Komissinskiy, P.; Kurian, J.; Schroeder, T.; Alff, L., Impact of oxygen stoichiometry on electroforming and multiple switching modes in TiN/TaOx/Pt based ReRAM. *Appl. Phys. Lett.* **2016**, *109* (17), 173503.
- 22. (a) H. Y. Lee; P. S. Chen; T. Y. Wu; Y. S. Chen; C. C. Wang; P. J. Tzeng; C. H. Lin; F. Chen; C. H. Lien; Tsai, M.-J., Low power and high speed bipolar switching with a thin reactive Ti buffer layer in robust HfO2 based RRAM. 2008 IEEE International Electron Devices Meeting 2008, 1-4; (b) A. Padovani; L. Larcher; P. Padovani; C. Cagli; Salvo, B. D., Understanding the role of the Ti metal electrode on the forming of HfO<sub>2</sub>-based RRAMs. 2012 4th IEEE International Memory Workshop **2012**, 1-4; (c) Chen, Y. Y.; Goux, L.; Clima, S.; Govoreanu, B.; Degraeve, R.; Kar, G. S.; Fantini, A.; Groeseneken, G.; Wouters, D. J.; Jurczak, M., Endurance/retention trade-off on HfO₂/metal cap 1T1R bipolar RRAM. IEEE Tran. Electron Devices 2013, 60 (3), 1114-1121; (d) Yalon, E.; Karpov, I.; Karpov, V.; Riess, I.; Kalaev, D.; Ritter, D., Detection of the insulating gap and conductive filament growth direction in resistive memories. Nanoscale 2015, 7 (37), 15434-15441; (e) Z. Wei; Y. Kanzawa; K. Arita; Y. Katoh; K. Kawai; S. Muraoka; S. Mitani; S. Fujii; K.Katayama; M. Iijima; T. Mikawa; T. Ninomiya; R. Miyanaga; Y. Kawashima; K. Tsuji; A. Himeno; T. Okada; R. Azuma; K. Shimakawa; H. Sugaya; T. Takagi; R. Yasuhara; K.Horiba; H. Kumigashira; Oshima, M., Highly reliable TaO<sub>x</sub> ReRAM and direct evidence of redox reaction mechanism. 2008 IEEE International Electron Devices Meeting 2008, 1-4; (f) Huang, J. J.; Kuo, C. W.; Chang, W. C.; Hou, T. H., Transition of stable rectification to resistive-switching in Ti/TiO<sub>2</sub>/Pt oxide diode. Appl. Phys. Lett. **2010**, 96 (26), 262901.

- 23. Bersuker, G.; Gilmer, D. C.; Veksler, D.; Kirsch, P.; Vandelli, L.; Padovani, A.; Larcher, L.; McKenna, K.; Shluger, A.; Iglesias, V.; Porti, M.; Nafría, M., Metal oxide resistive memory switching mechanism based on conductive filament properties. *J. Appl. Phys.* **2011**, *110* (12), 124518.
- 24. Xu, X.; Rajendran, B.; Anantram, M. P., Kinetic monte carlo simulation of interface-controlled hafnia-based resistive memory. *IEEE Trans. Electron Devices* **2020**, *67* (1), 118-124.
- 25. Song, H.; Kim, Y. S.; Park, J.; Kim, K. M., Designed memristor circuit for self-limited analog switching and its application to a memristive neural network. *Adv. Electron. Mater.* **2019**, *5* (6), 1800740.
- 26. Wu, Y.; Wang, X.; Lu, W. D., Dynamic resistive switching devices for neuromorphic computing. *Semiconductor Science and Technology* **2021**, *37* (2).